

Evaluating the de Hoffmann-Teller cross-shock potential at real collisionless shocks

Steven J Schwartz^{1*†}, Robert Ergun¹, Harald Kucharek², Lynn Wilson III³,
Li-Jen Chen³, Katherine Goodrich⁴, Drew Turner⁵, Imogen Gingell⁶, Hadi
Madanian⁷, Daniel Gershman³, Robert Strangeway⁸

¹Laboratory for Atmospheric and Space Physics, CU Boulder, Boulder, CO

²University of New Hampshire, Durham, NH

³Goddard Space Flight Center, Greenbelt, MD

⁴Space Sciences Laboratory, UC Berkeley, Berkeley, CA

⁵Space Exploration Sector, The Johns Hopkins Applied Physics Laboratory, Laurel, MD

⁶Physics and Astronomy, University of Southampton, Southampton, UK

⁷Southwest Research Institute, San Antonio, TX

⁸UCLA, Los Angeles, CA

Key Points:

- Measuring directly the cross-shock de Hoffmann-Teller potential in space is challenging.
- Proposed adaptive frame transformation techniques have limited utility for shocks with 2D or 3D time-varying structure.
- Electron inferences of the potential are robust but assume scattering is negligible.

Manuscript Date 26 Feb 2021

*Laboratory for Atmospheric and Space Physics, CU Boulder, Boulder, CO

†Also Emeritus Professor, Imperial College London

Abstract

Shock waves are common in the heliosphere and beyond. The collisionless nature of most astrophysical plasmas allows for the energy processed by shocks to be partitioned amongst particle sub-populations and electromagnetic fields via physical mechanisms that are not well understood. The electrostatic potential across such shocks is frame dependent. In a frame where the incident bulk velocity is parallel to the magnetic field, the deHoffmann-Teller frame, the potential is linked directly to the ambipolar electric field established by the electron pressure gradient. Thus measuring and understanding this potential solves the electron partition problem, and gives insight into other competing shock processes. Integrating measured electric fields in space is problematic since the measurements can have offsets that change with plasma conditions. The offsets, once integrated, can be as large or larger than the shock potential. Here we exploit the high-quality field and plasma measurements from NASA's Magnetospheric Multiscale mission to attempt this calculation. We investigate recent adaptations of the deHoffmann-Teller frame transformation to include time variability, and conclude that in practice these face difficulties inherent in the 3D time-dependent nature of real shocks by comparison to 1D simulations. Potential estimates based on electron fluid and kinetic analyses provide the most robust measures of the deHoffmann-Teller potential, but with some care direct integration of the electric fields can be made to agree. These results suggest that it will be difficult to independently assess the role of other processes, such as scattering by shock turbulence, in accounting for the electron heating.

Plain Language Summary

Shock waves form when a supersonic flow encounters an immovable object. Thus, ahead of the magnetic bubble formed by the Earth's extended magnetic field, the flow of charged particles emanating from the Sun known as the solar wind is shocked, slowed, and deflected around the Earth. In dense fluids, the conversion of the incident bulk flow energy into heat is accomplished by collisions between particles or molecules. However, the solar wind is so rarefied that such collisions are negligible, and the energy conversion involves more than one kinetic process that couples the different particles to the electromagnetic fields. In particular, electric potentials are believed to control the energy split between positive and negative particles. Measuring electric potentials in space is challenging because there is no available zero "earth" potential. In this work, we explore

54 alternative measurements of the potential associated with the electron physics. Some meth-
 55 ods can be made to agree with direct determinations using the measured electrons, but
 56 we conclude that despite the unprecedented data quality, they are not sufficient to pro-
 57 vide an independent determination of the potential. This poses challenges in assessing
 58 other, non-potential physics that also influences the electron energization.

59 1 Introduction

60 Shock waves in astrophysical plasma are almost always operating on scales that are
 61 much smaller than the particle collisional mean free path. Such collisionless shocks re-
 62 quire plasma kinetic processes to decelerate the incident bulk flow and “dissipate” that
 63 incident energy flux. These processes operate differently on the different plasma species
 64 and electromagnetic fields, and over different scales. They are responsible for preferen-
 65 tial heating together with the acceleration to high energies of sub-populations of parti-
 66 cles (Kucharek et al., 2003). This unknown partitioning of the incident energy lies at the
 67 heart of the shock problem. The bow shock formed by the interaction of the supersonic
 68 solar wind flow with the Earth’s magnetosphere has long been a prime laboratory for
 69 investigating collisionless shock physics thanks to its accessibility by ever-increasing high
 70 quality in situ satellite observations (Burgess & Scholer, 2015; Schwartz, 2006; Schwartz
 71 et al., 2013; Krasnoselskikh et al., 2013; Tsurutani & Stone, 1985; Stone & Tsurutani,
 72 1985; Scudder, Mangeney, Lacombe, Harvey, Aggson, et al., 1986).

73 Feldman et al. (1983) documented the non-Maxwellian nature of electron distri-
 74 butions seen at the bow shock and within the magnetosheath. They showed that the peak
 75 of the upstream solar wind distribution was accelerated toward the downstream region
 76 and eroded to leave a flat-topped sheath distribution. They noted that the solar wind
 77 flow is sub-thermal as far as the electrons are concerned, and established a framework
 78 in which electrons traverse, in both directions, a potential at the shock itself. Later work
 79 (C. C. Goodrich & Scudder, 1984; Scudder, 1987; Thomsen, Gosling, et al., 1987) pointed
 80 out that the potential seen by these electrons is not the same as that which slows down
 81 the solar wind ions. In the traditional “Normal Incidence” (NIF) frame, in which the up-
 82 stream flow is directed along the shock normal, the magnetized electrons drift along the
 83 shock surface, giving up energy to the motional $-\mathbf{V} \times \mathbf{B}$ electric field.

84 de Hoffmann and Teller (1950) employed a different shock frame for their studies
85 of MHD shock waves. This “deHoffmann-Teller” (HT) frame slides along the shock front
86 (to keep the shock at rest) so that the upstream fluid velocity is aligned along the mag-
87 netic field. Faraday’s Law ensures that this is also the case in the downstream region.
88 The HT frame has been used in studies of shock ion reflection (Sonnerup, 1969; Schwartz
89 et al., 1983), electron “heating” (Scudder, Mangeney, Lacombe, Harvey, Wu, & Ander-
90 son, 1986; Thomsen, Mellott, et al., 1987; Schwartz et al., 1988) and magnetopause re-
91 connection (Khrabrov & Sonnerup, 1998; Paschmann et al., 2018) amongst others. Par-
92 ticle energetics are simplified in the HT frame. From the brief discussion above, we see
93 that the energy gained (or lost) by an electron traversing the shock provides a direct mea-
94 sure of the electrostatic potential in the HT frame, so that the electron behavior and HT
95 fields are intrinsically coupled. Establishing the parametric dependence of the HT po-
96 tential would solve the shock partition problem as far as electron energization is concerned.

97 Measuring the cross-shock potentials directly is difficult in space due to calibra-
98 tion uncertainties in a floating potential environment, the absence or imbalance of full
99 3D electric antennae, and other considerations. Attempts to do so are limited (Dimmock
100 et al., 2012; Cohen et al., 2019; Hanson et al., 2019). Electron kinetic observations pro-
101 vide proxy methods to evaluate the HT potential (Scudder, Mangeney, Lacombe, Har-
102 vey, Wu, & Anderson, 1986; Schwartz et al., 1988; Lefebvre et al., 2007). These prox-
103 ies, however, cannot fully disentangle the role of such DC fields in inflating the electron
104 distributions, from the influences of wave-particle scattering (Wilson et al., 2014; Stasiewicz
105 & Eliasson, 2020), magnetic pumping (Lichko & Egedal, 2020) and other process that
106 have been suggested to play a role in the electron physics. Additionally, 3D global as-
107 pects such as curvature (Mitchell & Schwartz, 2013, 2014), and shock ripples (Johlander
108 et al., 2016) can influence the HT potential and electron dynamics. There is a gulf be-
109 tween the idealized 1D steady MHD shocks for which the HT frame was invented, and
110 the dynamic, temporally and spatially varying shocks observed in space.

111 Comișel et al. (2015), revisited by Marghitu et al. (2017) (hereafter C&M), com-
112 pared direct integration of the HT potential in a 1D particle in cell simulation with the
113 electron behavior, and concluded that the standard HT transformation by a constant
114 velocity along the shock front resulted in HT potentials that disagreed with that inferred
115 by the electron behavior, being both larger in magnitude and opposite in sign in their
116 simulations. They introduced an “Adaptive Hoffmann-Teller” (AHT) transformation that

117 varied with space through the shock layer in such a way that the local, instantaneous
 118 motional electric field vanished. Although this is no longer a true reference frame, they
 119 showed that this AHT approach agreed well with the electron determinations of the HT
 120 potential profile.

121 This intriguing result opens up the question about whether such an adaptive ap-
 122 proach can also work with spacecraft observations of real shocks. We address this ques-
 123 tion here using the unprecedented high quality field and particle data from NASA’s Mag-
 124 netospheric Multiscale (MMS) mission.

125 The next sections summarize the data and our primary analysis methods. We then
 126 present our Results and provide some Discussion before drawing our final Conclusions.

127 **2 Data**

128 Our primary results are drawn from the Magnetospheric Multiscale mission (MMS)
 129 (Burch et al., 2016). We also used data from both the Wind (Harten & Clark, 1995; Wil-
 130 son et al., 2021) and ARTEMIS (Angelopoulos, 2010) spacecraft to establish the prevail-
 131 ing interplanetary conditions. The main analysis relies on MMS data from the Fast Plasma
 132 Investigation (FPI) (Pollock et al., 2016), Fluxgate Magnetometer (FGM) (Russell et
 133 al., 2016) and electric field instrumentation (Torbert et al., 2016; Ergun et al., 2016; Lindqvist
 134 et al., 2016). We are interested in the quasi-static (DC) electric shock potential. Deduc-
 135 ing this from the direct measurement of the 3D electric field (\mathbf{E}) by MMS is complicated
 136 by a baseline offset which, when integrated, can be as large or larger than the shock po-
 137 tential. The shorter spin-axis sensors contribute a raw baseline offset up to ~ 3 mV/m
 138 in the plasma conditions we are investigating (Ergun et al., 2016). A small (< 0.5 mV/m)
 139 baseline offset in the spin plane of the spacecraft comes from a sunward-directed elec-
 140 tric field due to a small imbalance of photoelectron currents (Lindqvist et al., 2016). These
 141 offsets can change if the plasma conditions change. The medium-term (many minutes)
 142 electric field offset is routinely removed by a calibration procedure that compares \mathbf{E} to
 143 $\mathbf{V} \times \mathbf{B}$ and assumes the median of $\mathbf{E} \cdot \mathbf{B} = 0$ over several minutes. A short-term (4 s)
 144 offset correction, the median (not average) of $\mathbf{E} \cdot \mathbf{B} = 0$, is applied to E_{\parallel} to correct for
 145 changing plasma conditions. The remaining baseline offsets in \mathbf{E} can be as high as 0.5 mV/m
 146 but are often less. We shall see that one way to represent the shock potential of inter-
 147 est is entirely through E_{\parallel} .

148 Figure 1 summarizes the configuration of the MMS spacecraft on 2019-03-05. As
 149 can be seen in Figure 1b, during this period the spacecraft were co-linear along their com-
 150 mon orbit with separations from 100–700 km. They traversed the Earth’s bow shock trav-
 151 eling almost exactly along the shock normal. An overview of the plasma observations
 152 is given in the left of Figure 2 with a zoomed view spanning ~ 3 min given in Figure 2
 153 (right). The FPI plasma instrumentation is not optimized for measuring the cold solar
 154 wind ion beam nor the cool solar wind electrons, which adds both noise and uncertainty
 155 to these measurements. The extended disturbed region upstream (later times) of the shock
 156 is due to the presence of reflected ions in the shock foot and its extension or reformation
 157 tion, visible after 19:40:00. That reformation structure occurs simultaneously on all four
 158 spacecraft (see Figure 1) with systematically growing amplitude. Interestingly, even at
 159 MMS1 where this feature is relatively small in magnetic field and density, for example,
 160 the electric fields there (panels (i) and (j) of Figure 2) are comparable in amplitude to
 161 that at the main shock ramp at 19:39:30 (cf. Wilson et al. (2014)).

162 Table 1 summarizes the underlying solar wind conditions and derived shock param-
 163 eters. We have drawn on solar wind data from the Wind spacecraft, lagged by 65 min-
 164 utes from Wind’s upstream location to the nose of the bow shock. In view of its criti-
 165 cal role in our analysis, we use a local MMS measurement to characterize the upstream
 166 magnetic field, which is within 7 degrees of that observed by Wind. We use an emper-
 167 ical shock model (Slavin & Holzer, 1981; Schwartz, 1998) to determine the direction of
 168 the shock normal.

169 The times of the shock crossing at the different spacecraft are indicated by the ver-
 170 tical dashed lines in Figure 1c-f, which intersect the mid-points of the full shock ramp
 171 field profiles. MMS3 (Figure 1f) exited the magnetosheath briefly as the shock motion
 172 stalled and reversed, before a final exit at 19:45. Table 1 shows that the derived shock
 173 speed along the normal was almost the same between the first ($2 \rightarrow 1$) and second ($1 \rightarrow$
 174 4) spacecraft pairs before slowing down as MMS3 encountered it. In our analysis we will
 175 draw primarily on data from MMS1 during the middle of the nearly constant shock mo-
 176 tion.

Table 1. Solar wind and shock parameters

Parameter	Value	Units	Comments
MMS2 Shock Crossing Time	2019-03-05 19:39:05	UT	
MMS2 Location	(10.1, -13.4, 6.85)	GSE R_e	
Upstream field \mathbf{B}_{up}	(3.45, 2.47, -2.46)	GSE nT	MMS2 19:43:57–19:44:47
Proton density $n_{p,up}$	3.5	cm^{-3}	Wind 3DP [†]
Proton velocity $V_{p,up}$	(-402, 14, -5)	km/s	Wind 3DP
Proton temperature $T_{p,up}$	5.9	eV	Wind 3DP
Electron temperature $T_{e,up}$	4.4	eV	Wind 3DP
Plasma beta β_{up}	0.6		total
Shock normal \mathbf{n}	(0.847, -0.482, 0.226)	GSE	(Slavin & Holzer, 1981)
θ_{Bn}	76	deg	
Inflow speed along \mathbf{n} : V_n	-341	km/s	In shock rest frame
Shock Alfvén Mach M_A	6.0		
Fast Magnetosonic Mach M_f	4.9		
Spacecraft separations:			$\mathbf{r}_{21} \equiv \mathbf{r}_1 - \mathbf{r}_2$, etc.
$\mathbf{r}_{21} \cdot \mathbf{n}$	-201	km	
$\mathbf{r}_{14} \cdot \mathbf{n}$	-104	km	
$\mathbf{r}_{43} \cdot \mathbf{n}$	-407	km	
Shock motion along \mathbf{n} :			$\mathbf{r}_{21} \cdot \mathbf{n}/(t_1 - t_2)$, etc.
$V_{shkn,2 \rightarrow 1}$	-7.4	km/s	
$V_{shkn,1 \rightarrow 4}$	-7.8	km/s	
$V_{shkn,4 \rightarrow 3}$	-1.3	km/s	First encounter

[†]All Wind parameters are 20 minute averages lagged 65 minutes.

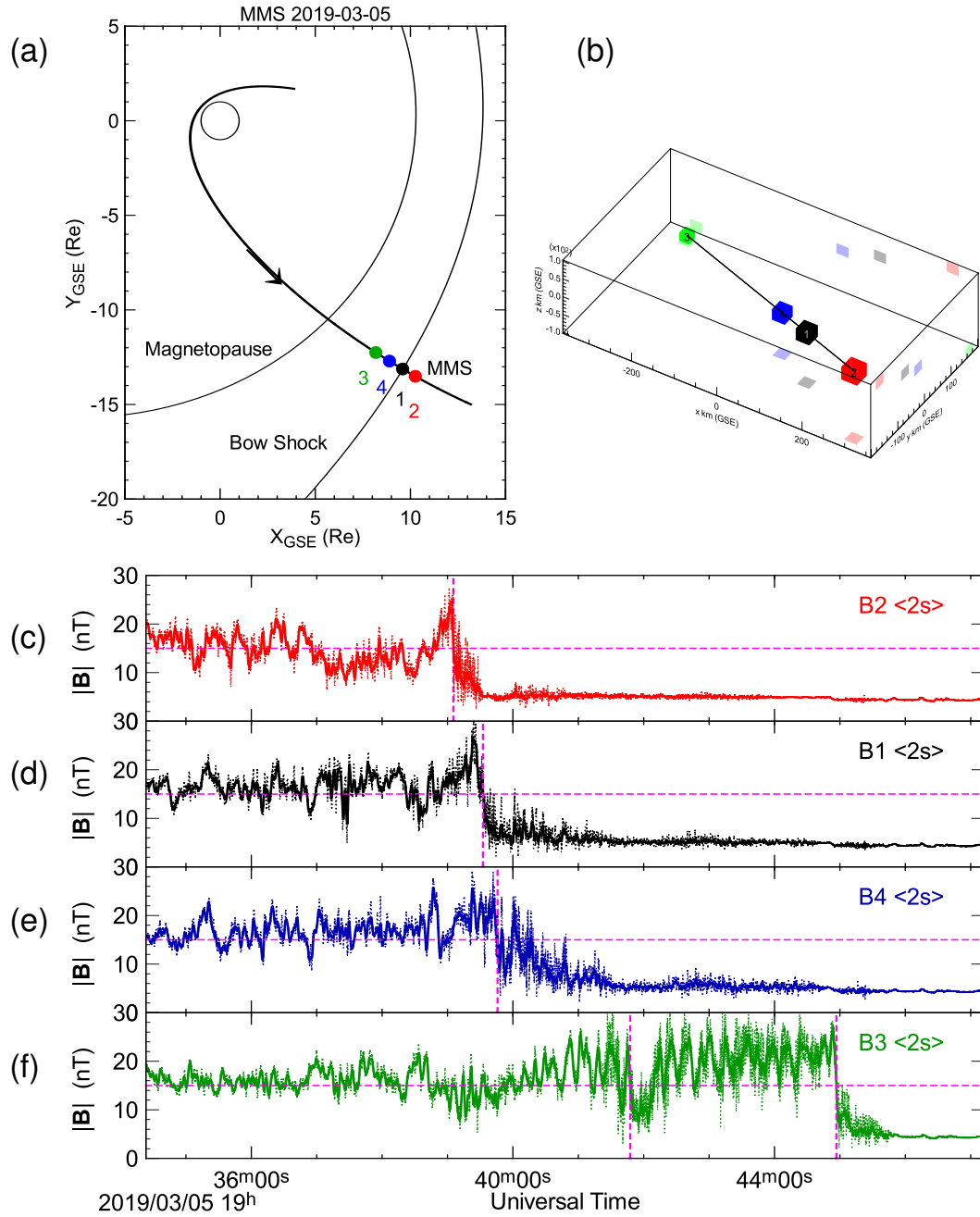


Figure 1. Configuration of MMS on 2019-03-05. (a) MMS orbit outbound through the bow shock, showing the relative positions of MMS1-4. (b) Detailed relative positions of the four MMS spacecraft, showing their co-linear alignment which is along the orbit and therefore, from (a) essentially along the shock normal. (c)-(f) Magnetic field magnitudes measured by the four spacecraft (dotted = full resolution; solid = 2 s averages). The times corresponding to the mid-point of the shock ramps are located by the intersections of the dashed horizontal and vertical lines in each panel. MMS3 (f) exited the magnetosheath briefly at $\sim 19 : 41 : 48$ and for the second time at $\sim 19 : 44 : 56$.

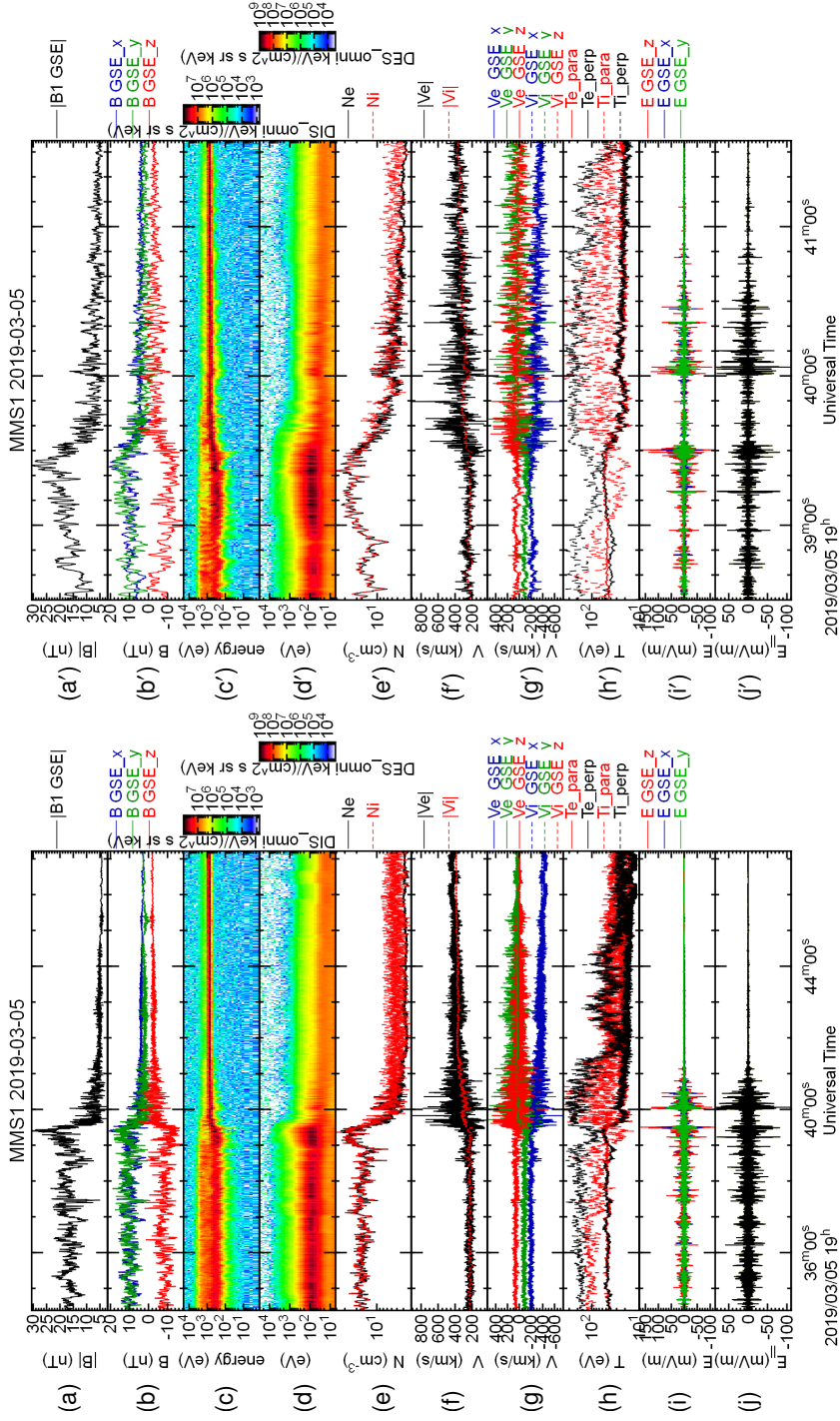


Figure 2. Overview (L) and detail (R) of the shock crossing by MMS on 2019-03-05 used in this study. All data are from MMS1 and taken in burst mode. (a),(b) magnetic field magnitude and components (c), (d) ion and electron omni-directional energy spectra (e) electron and ion number densities (f), (g) ion and electron bulk velocity magnitudes and components (h) electron (solid) and ion (dashed) temperatures along (red) and perpendicular (black) to the local magnetic field (i) DC electric field components and (j) DC field E_{\parallel} along the magnetic field.

3 Background and methodology

3.1 Shock reference frames

We review the subject of electric fields at a shock here. We employ the standard 1D shock lmn coordinate system in which the shock normal \mathbf{n} points into the upstream (unshocked) region, the upstream magnetic field \mathbf{B}^{up} lies in the ln plane with $B_l^{up} > 0$, and \mathbf{m} completes the right-handed system. For steady 1D shocks, the downstream field should also lie in the ln plane, and in both NIF and HT frames the normal, field and bulk flow velocities up- and downstream are coplanar. In the NIF frame, the motional $-\mathbf{V} \times \mathbf{B}$ electric field is along $+\mathbf{m}$ and, in steady-state applications, is spatially uniform. In the derivations below, we use subscripts to denote component and species labels. Superscripts are reserved for descriptive labeling and reference frame designation.

Collisionless particle motion is controlled by electromagnetic fields that are self-consistent with the particle charge density and currents. However, the electric field is not invariant under Galilean transformation, and so analysis must specify the frame of reference being used. Although the classic shock in a collisional fluid is usually analyzed in the Normal Incidence Frame (NIF), in which the shock is at rest and the incident bulk flow is directed along the shock normal, de Hoffmann and Teller (1950) noticed that in a magnetized plasma there are benefits to transforming to a frame in which the bulk flow is directed along the magnetic field. Faraday's Law ensures that in this frame this will be true in both the upstream and downstream regions, as the m -component of \mathbf{E} is zero and continuous. In this deHoffmann-Teller (HT) frame, the motional $-\mathbf{V} \times \mathbf{B}$ electric field vanishes, which makes particle motion and energetics particularly simple. It has been employed in studies of particle energization at shocks (Sonnerup, 1969; Thomsen et al., 1983; Schwartz et al., 1983; Wu, 1984), in electron heating at shocks (Scudder, Mangeney, Lacombe, Harvey, Aggson, et al., 1986; Thomsen, Mellott, et al., 1987; Schwartz et al., 1988; Lefebvre et al., 2007), and plays a central role in other phenomena, such as magnetic reconnection (Khrabrov & Sonnerup, 1998).

3.2 Shock electric fields

In the HT frame at steady 1D shocks, the only electric field is within the shock layer itself, directed outward along the shock normal, and is intimately related to the electron fluid behavior as evidenced by considering the electron momentum equation, which in

208 an arbitrary reference frame can be cast as:

$$\mathbf{E}^{ve} \equiv \mathbf{E} + \mathbf{V}_e \times \mathbf{B} = -\frac{1}{en_e} \nabla \cdot \underline{\mathbf{P}}_e + \text{inertial, frictional, ...} = \mathbf{E}^{amb} + \text{other terms} \quad (1)$$

209 Within the shock layer, the electron bulk flow velocity \mathbf{V}_e drifts in the m -direction rel-
 210 ative to that of the ions, but stays nearly parallel to the magnetic field in the HT frame
 211 (Scudder, 1987). That drift, however, when viewed in the NIF frame, is along the up-
 212 stream motional electric field and results in the electron NIF energization being substan-
 213 tially less than the ion energy loss to the NIF cross-shock potential (C. C. Goodrich &
 214 Scudder, 1984).

215 The leading term on the right hand side of Equation 1 is the frame invariant am-
 216 bipolar electric field. In the HT shock rest frame the left hand side is simply the elec-
 217 tric field \mathbf{E}^{HT} , since $\mathbf{V}_e \parallel \mathbf{B}$, which is directed along the shock normal since the off-
 218 diagonal terms of the electron pressure tensor, together with the inertial terms, are typ-
 219 ically much smaller than the diagonal terms. It is also possible to project that electric
 220 field along the magnetic field by dotting with \mathbf{B} . The invariance of $\mathbf{E} \cdot \mathbf{B}$ confirms the
 221 frame invariance of the result:

$$E_{\parallel} = -\frac{1}{en_e} (\nabla \cdot \underline{\mathbf{P}}_e) \cdot \mathbf{B} / B \quad (2)$$

222 so that

$$\mathbf{E}^{amb} = -\frac{\mathbf{n}}{en_e} (\nabla \cdot \underline{\mathbf{P}}_e) \cdot \mathbf{B} / B_n \quad (3)$$

223 The transformation velocity \mathbf{V}^{α} from a shock rest frame into the HT frame is found
 224 by finding the frame in which the flow and field are aligned, or equivalently in which the
 225 components of \mathbf{E} tangential to the shock vanish. C&M do this by looking at the specific
 226 E_l and E_m expressions under frame transformation. These considerations can be encap-
 227 sulated in the following compact form:

$$\mathbf{V}^{T,\alpha} = -\mathbf{n} \times \mathbf{E}^{T,\alpha} / B_n^{T,\alpha} \quad (4)$$

228 where we have used the superscript “ T, α ” to denote parameters associated with the trans-
 229 formation to the α -frame in anticipation of the possible alternatives developed below.
 230 Interestingly, this formulation of $\mathbf{V}^{T,\alpha}$ will yield an electric field $\mathbf{E}^{\alpha} = \mathbf{E} + \mathbf{V}^{T,\alpha} \times \mathbf{B}$
 231 that is associated with the frame invariant ambipolar field regardless of the initial frame

232 of reference. However, since by construction $\mathbf{V}^{T,\alpha}$ is perpendicular to the shock normal
 233 \mathbf{n} , it will only transform to the origin of the HT frame if the shock is at rest in the ini-
 234 tial frame.

235 Although it is both possible and practical to transform fields directly from the space-
 236 craft frame of reference to the HT frame and its adapted variants, in expositions below
 237 we start from the NIF frame, which moves relative to the spacecraft frame at a veloc-
 238 ity

$$\begin{aligned}\mathbf{V}^{SC2NIF} &= V_n^{sh} \mathbf{n} + \mathbf{n} \times (\mathbf{V}^{up,SC} \times \mathbf{n}) \\ &= V_n^{sh} \mathbf{n} + \mathbf{V}^{up,SC} - \mathbf{n} (\mathbf{V}^{up,SC} \cdot \mathbf{n})\end{aligned}\quad (5)$$

239 where V_n^{sh} is the shock velocity relative to the spacecraft along the shock normal, and
 240 $\mathbf{V}^{up,SC}$ is the constant upstream (“up”) flow velocity measured in the spacecraft frame.
 241 From (5) we see that the upstream flow velocity in the NIF frame is purely along the shock
 242 normal, since

$$\begin{aligned}\mathbf{V}^{up,NIF} &= \mathbf{V}^{up,SC} - \mathbf{V}^{SC2NIF} \\ &= \mathbf{V}^{up,SC} - V_n^{sh} \mathbf{n} - \mathbf{V}^{up,SC} + \mathbf{n} (\mathbf{V}^{up,SC} \cdot \mathbf{n}) \\ &\equiv V_n^{up} \mathbf{n}\end{aligned}\quad (6)$$

243 where V_n^{up} is the component of the upstream flow velocity along the shock normal in the
 244 NIF, or any other, shock rest frame. We then find the NIF electric field as

$$\mathbf{E}^{NIF} = \mathbf{E}^{SC} + \mathbf{V}^{SC2NIF} \times \mathbf{B} \quad (7)$$

245 Starting from the NIF frame, the electric field following transformation using $\mathbf{V}^{T,\alpha}$
 246 from (4) is

$$\mathbf{E}^\alpha(t) = \mathbf{E}^{NIF}(t) + \mathbf{V}^{T,\alpha} \times \mathbf{B}(t) \quad (8)$$

$$= \mathbf{E}^{NIF}(t) - (\mathbf{n} \times \mathbf{E}^{T,\alpha} / B_n^{T,\alpha}) \times \mathbf{B}(t) \quad (9)$$

$$= \mathbf{E}^{NIF}(t) - \mathbf{E}^{T,\alpha} B_n(t) / B_n^{T,\alpha} + \mathbf{n} (\mathbf{E}^{T,\alpha} \cdot \mathbf{B}(t)) / B_n^{T,\alpha} \quad (10)$$

247 where we have shown the time dependence as a shorthand for both spatial and tempo-
 248 ral dependencies of the fields. In the adaptive forms introduced by C&M, some of the
 249 ingredients in $\mathbf{V}^{T,\alpha}$ are also not constant. We shall assume throughout that the shock
 250 normal \mathbf{n} is constant (see Section 5).

251 In general, the action of the middle term in equation 10 attempts primarily to can-
 252 cel out the NIF tangential field components. The field along \mathbf{n} involves all three terms
 253 to some extent. So, for example, the traditional transformation from the NIF frame to
 254 the HT one uses upstream values for the transformation to yield

$$\mathbf{E}^{T,HT} = -V_n^{up} \mathbf{n} \times \mathbf{B}^{up} \quad \text{with} \quad B_n^{T,HT} = B_n^{up} \quad (11)$$

$$\mathbf{V}^{T,HT} = +\mathbf{n} \times (V_n^{up} \mathbf{n} \times \mathbf{B}^{up}) / B_n^{up} \quad (12)$$

$$\mathbf{E}^{HT} = \mathbf{E}^{NIF}(t) + V_n^{up} \mathbf{n} \times \mathbf{B}^{up} \frac{B_n(t)}{B_n^{up}} - \mathbf{n} (V_n^{up} \mathbf{n} \times \mathbf{B}^{up}) \cdot \mathbf{B}(t) / B_n^{up} \quad (13)$$

255 For strictly 1D shocks, B_n is constant in space and time, so the fraction in the middle
 256 term of Equation 13 is unity. This term then cancels the NIF upstream tangential (m -
 257 component) electric field. From the last term we see that the normal component of \mathbf{E}^{HT}
 258 is the same as that in the NIF frame unless the local magnetic field has a non-zero com-
 259 ponent along this $\mathbf{m} \equiv \mathbf{n} \times \mathbf{l}$ direction. This role of non-coplanar magnetic fields within
 260 the shock layer in making the cross-shock electric fields, and hence potentials, different
 261 in the HT and NIF frames is at the heart of this subject (C. C. Goodrich & Scudder,
 262 1984; Thomsen, Gosling, et al., 1987)

263 C&M introduced an adaptive approach which followed variations of the fields by
 264 using a non-constant local frame transformation to remove the tangential electric field
 265 at every point. Their method (see Marghitu et al. (2017) Equation 5b) in our framework
 266 simply uses the local electric field in the NIF frame with Equation 4, which yields the
 267 following set of relations:

$$\mathbf{E}^{T,AHT} = \mathbf{E}^{NIF}(t) \quad \text{with} \quad B_n^{T,AHT} = B_n^{up} \quad (14)$$

$$\mathbf{V}^{T,AHT}(t) = -\mathbf{n} \times \mathbf{E}^{NIF}(t) / B_n^{up} \quad (15)$$

$$\mathbf{E}^{AHT} = \mathbf{E}^{NIF}(t) \left(1 - \frac{B_n(t)}{B_n^{up}} \right) + \mathbf{n} (\mathbf{E}^{NIF}(t) \cdot \mathbf{B}(t)) / B_n^{up} \quad (16)$$

268 In the 1D case applicable to C&M's simulations the first term in Equation (16) vanishes
 269 leaving \mathbf{E}^{AHT} with only a normal component related explicitly to the frame-invariant
 270 parallel electric field as it should. In the 2D and 3D case, where the magnetic field com-
 271 ponent along the (assumed) constant normal direction varies, Equation (16) shows that
 272 not only is that cancellation of the tangential electric field in the first term imperfect,
 273 but that there can also be an influence on the normal component E_n^{AHT} from this term
 274 that can be significant and of varying sign depending on the instantaneous $B_n(t)$. We
 275 shall see later that this influence and related considerations suggest that seeking an ap-

276 appropriate frame transformation velocity of any kind is less satisfactory than methods which
 277 either use proxies for the electric field in the HT frame, or which focus from the outset
 278 on the parallel electric field directly.

279 The formal cancellation problem can be alleviated by extending the AHT to use
 280 the full time/space dependent fields. Simply insert $B_n(t)$, in the frame transformation
 281 specification (Equations (14)–(15)) in place of the constant B_n^{up} in those equations, and
 282 hence in Equation (16). We call this the “AHTt” transformation. It solves the tangential
 283 field problem at the expense of making \mathbf{E}^{AHTt} proportional to $1/B_n(t)$ which, un-
 284 like the 1D case, can lead to singularities:

$$\mathbf{E}^{AHTt} = \mathbf{n} (\mathbf{E}^{NIF}(t) \cdot \mathbf{B}(t)) / B_n(t) \quad (17)$$

285 3.3 Shock potentials

286 Armed with estimators \mathbf{E}^α of the electric field in the HT frame, the potential profile
 287 in the HT frame can be found by integration through the shock layer:

$$\phi^\alpha(n) = - \int^n E_n^\alpha(t) dn = - \int^\ell E_\parallel^\alpha(t) d\ell \quad (18)$$

288 where n and ℓ are coordinates along the shock normal and magnetic field respectively.
 289 We use the multiple spacecraft observations to determine the shock velocity V_n^{sh} along
 290 the normal relative to the spacecraft. This enables us to write $dn = -V_n^{sh} dt$ and hence
 291 we evaluate the potential profile

$$\phi^\alpha(t) = V_n^{sh} \int_{t_o}^t E_n^\alpha(t) dt \quad (19)$$

292 up to some arbitrary constant.

293 C&M evaluated the standard ϕ^{HT} directly from the electric fields in their simu-
 294 lations based on these steady state formulations and found that it gave poor agreement
 295 with the electron behavior, even to the extent of implying the electrons should deflate
 296 (“cool”) in their simulation instead of the observed inflation. Although there can be sig-
 297 nificant differences in the nature electric fields in simulation vs. nature (Wilson et al.,
 298 2021) the electron behavior should always be self-consistent with the fields in both cases.
 299 They cross-checked the electron response by Liouville mapping the electron distributions
 300 (Scudder, Mangeney, Lacombe, Harvey, Wu, & Anderson, 1986; Lefebvre et al., 2007;
 301 Schwartz et al., 1988), and also calculated the integrated ambipolar field directly.

302 The adaptive extension of HT analysis to time-varying systems worked well in the
 303 simulations reported by C&M. However, careful inspection of the derivation shown here
 304 reveals that the application to 2D or 3D time-variable shocks is both unclear and danger-
 305 ridden. In the 1D case, both the shock normal \mathbf{n} and, thanks to $\nabla \cdot \mathbf{B} = 0$, the nor-
 306 mal component of the magnetic field B_n are constants. In 2D or 3D, allowing B_n to vary
 307 in time opens up the possibility for incomplete cancellation of \mathbf{E}^{NIF} in Equation (16)
 308 or large jumps in $\phi^{AHTt}(t)$ whenever the local B_n passes through or close to zero. We
 309 have not found an approach that enables $\mathbf{n}(t)$ to be determined, nor is there any guar-
 310 antee that B_n would be better behaved if we did. Below we compare the various esti-
 311 mators of ϕ using high quality in situ spacecraft data. None of these methods overcomes
 312 the intrinsic difficulty of measuring DC-coupled electric fields in space over the scales of
 313 a shock traversal.

314 3.4 Electron behavior

315 For nearly all shocks in the heliosphere, the bulk flow velocities, together with the
 316 shock velocities, are much smaller than the electron thermal speeds. In the absence of
 317 collisions, electrons travel along the field lines in both directions across the shock. Those
 318 traveling into the shock from the upstream (unshocked) side get accelerated by the HT
 319 potential while those traveling away from the shock get decelerated. This leads to elec-
 320 tron distributions that are “inflated”, (Scudder, Mangeney, Lacombe, Harvey, Wu, & An-
 321 derson, 1986; Scudder, 1995) i.e., broader - in both directions - in the downstream re-
 322 gion than in the upstream one, giving the impression that the electrons are heated from
 323 upstream to downstream. While this is the consequence at the fluid level, it is clear that
 324 the collisionless particle behavior is more subtle.

325 The inflation of electron phase space is linked to the HT cross-shock potential, ϕ^{HT} ,
 326 which is found by integrating \mathbf{E}^{HT} across the shock. In a shock rest frame this poten-
 327 tial will be path independent, and can be found by integrating, e.g., along the shock nor-
 328 mal. A magnetized electron will follow the field line, and its energization is equivalent
 329 to integrating the parallel projection of \mathbf{E} along the field line. It is important to recall
 330 that the bulk flow velocity is small compared to the electron thermal speed. Electrons
 331 from the downstream region can overcome the potential and lose kinetic energy as they
 332 emerge to stream upstream away from the shock.

333 We also exploit the electron single particle behavior described above to calculate
 334 $\phi^{Liouville}$ using Liouville's Theorem. We perform this by transforming the electron dis-
 335 tribution functions into the steady-state HT frame based on upstream plasma param-
 336 eters. We average the distribution function $f(v_{\parallel})$ within the upstream region to use as
 337 a reference distribution $f^{ref}(v_{\parallel})$, that we then represent by fitting a κ -distribution. For
 338 each measured $f(v_{\parallel}, t)$ we find the local $\phi(t)$ that minimizes the least squares difference
 339 between f^{ref} shifted by an energy $e\phi(t)$ and the measured ones over a range of values
 340 of f that correspond to being close to but beyond the edge of the downstream flattopped
 341 distribution. We do this separately for electrons traveling parallel to the magnetic field,
 342 corresponding in our example to electrons traveling upstream, and anti-parallel electrons.

343 Note that this procedure maps incoming electron trajectories forward in time and
 344 outgoing electrons backward in time from the f^{ref} to $f(v_{\parallel}, t)$. Technically, Liouville's
 345 theorem requires following each electron trajectory to other points on that same trajec-
 346 tory. In addition to time-variability, those trajectories also drift tangentially along the
 347 shock surface (C. C. Goodrich & Scudder, 1984). We assume here that the distributions
 348 are quasi-steady in time and space in order to use a snapshot of the upstream distribu-
 349 tion to map to all other locations and times. We assume that the electrons conserve their
 350 first adiabatic invariant, namely their magnetic moments μ_m . We focus on field-aligned
 351 electrons with $\mu_m = 0$ as this removes dependency on the magnetic profile.

352 One example of this procedure is shown in Figure 3 below. The effect of the HT
 353 velocity transformation can be seen in the asymmetry at low energies and by the steeper
 354 (shallower) $f(v)$ in the anti-parallel (parallel) direction. Phase space densities above the
 355 flat-top values in the anti-parallel direction are probably also contaminated by secondary
 356 or photoelectrons of spacecraft origin. The mapped distributions (black) fit the paral-
 357 lel electron distribution well. The anti-parallel mapping fit is poorer. It is not clear if
 358 this can be attributed to the uncertainties in or influence of the HT transformation, or
 359 if other energization mechanisms operate specifically on the incoming (anti-parallel) elec-
 360 tron population. The lower panel of Figure 3 shows $\phi^{Liouville}$ for the separate popula-
 361 tions and the location of the reference distribution (magenta interval) and the example
 362 instance used in the top panel. Generally, the anti-parallel $\phi^{Liouville}$ is noisier, although
 363 both potentials agree well through the main shock ramp. The Liouville mapping esti-
 364 mator for ϕ is unique in that it does not require an explicit spatial integral and thus is
 365 immune to errors in determination of the shock speed.

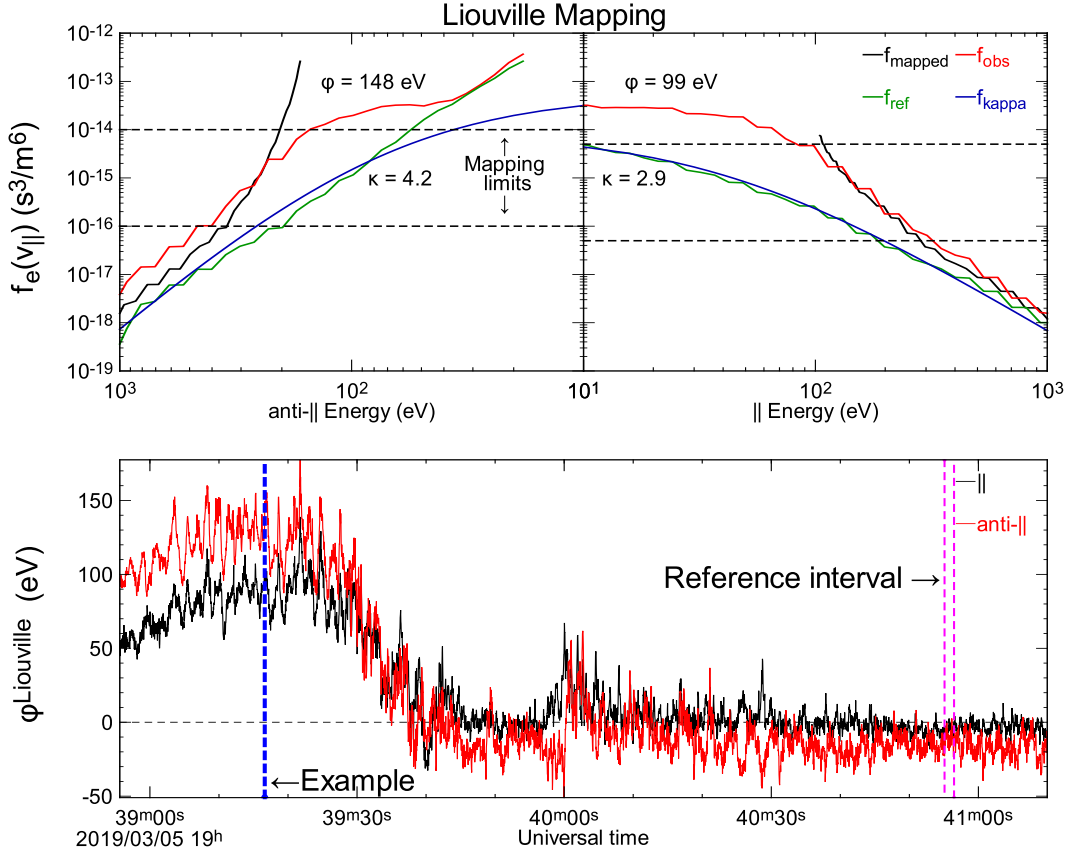


Figure 3. Illustration of the Liouville mapping determination of the deHoffmann-Teller potential. The top panel shows the reference distribution (green) which is an average of electrons travelling with pitch angles in the range $0 - 30^\circ$ or $150 - 180^\circ$ over the interval delineated by the magenta dashed lines in the lower panel. The blue curves show the κ -distribution fits to those reference distributions. The least squares method of mapping within the dashed mapping limits result in a shift of the reference distribution to the black f_{mapped} . This example was drawn from the time downstream of the shock overshoot indicated by the dashed blue line in the bottom panel. The bottom panel shows the time series of $\phi(t)$ determined by repeating this process for all times separately for electrons within 30° of being field-aligned (black) and anti-parallel (red) populations. All data are drawn from MMS1.

3.5 Summary of ϕ^{HT} estimators

The analysis and derivations performed in the previous sub-sections lead to a number of possible estimations of the cross-shock de Hoffmann-Teller potential. We employ several alternatives for illustration and comparison purposes. Specifically, we calculate:

$$1. \phi^{HT} = V_n^{sh} \int E_n^{HT}(t) dt \equiv V_n^{sh} \int (\mathbf{E}^{NIF}(t) + \mathbf{V}^{T,HT} \times \mathbf{B}^{up}) \cdot \mathbf{n} dt$$

using Equation (11) or (12). This is the traditional method using static upstream values for the (constant) frame transformation velocity.

$$2. \phi^{AHT} = V_n^{sh} \int (\mathbf{E}^{NIF}(t) + \mathbf{V}^{T,AHT}(t) \times \mathbf{B}(t)) \cdot \mathbf{n} dt$$

using Equation (14) or (15). This is the conservative application of C&M's adaptive de Hoffmann-Teller transformation, with a time dependent transformation velocity but retaining $B_n = \text{constant}$.

$$3. \phi^{AHTt} = V_n^{sh} \int (\mathbf{E}^{NIF}(t) + \mathbf{V}^{T,AHTt}(t) \times \mathbf{B}(t)) \cdot \mathbf{n} dt$$

which is the full naïve application of the adaptive transformation that uses $B_n(t)$ in the frame transformation to reach Equation (17).

$$4. \phi^{\parallel} = - \int E_{\parallel}(t) d\ell \equiv V_n^{sh} \int E_{\parallel}(t) B^{up} / B_n^{up} dt$$

which is a direct integration of the special $E_{\parallel}(t)$ data product provided by the electric fields instrument team. This does not require the calculation of a frame transformation thanks to the frame invariance of E_{\parallel} . However, we employ static upstream fields and a determination of the shock normal velocity V_n^{sh} in the spacecraft frame to convert from dn to $d\ell$. This enables a direct comparison with ϕ^{HT} . Additionally, this calculation does not require any down-sampling of the electric field to the cadence of other measurements.

$$5. \phi^{ve} = V_n^{sh} \int (\mathbf{E}(t) + \mathbf{V}_e(t) \times \mathbf{B}(t)) \cdot \mathbf{n} dt$$

which integrates the left hand side of the electron momentum equation (1). Despite the fact that this electric field is evaluated in the electron frame rather than a shock rest frame, it is equivalent to the ambipolar \mathbf{E}^{amb} from equation (3) and hence can be integrated to estimate ϕ^{HT} . Unlike the various forms using $V^{T,\alpha}$, ϕ^{ve} integrates quantities measured in the spacecraft frame without any additional frame transformations.

$$6. \phi^{amb} = \int \frac{1}{en_e} \frac{dP_{e,nn}}{dt} dt$$

which is a direct integration of the right hand side of the electron momentum equation (1) again assuming that the diagonal pressure term dominates. Note that the

398 shock velocity does not appear here as the spatial integration of the weighted spa-
 399 tial derivative of $P_{e,nn}$ is converted directly into the time domain.

400 7. ϕ^{LvI0} ,

401 the Liouville-mapped determination of ϕ as described in the preceding section and
 402 illustrated in Figure 3. We use the parallel rather than anti-parallel estimator as
 403 discussed in relation to Figure 3. Unlike the other estimators of ϕ , ϕ^{LvI0} is not the
 404 result of an integration; it provides the absolute potential relative to the location
 405 of the reference $f^{ref}(v_{||})$.

406 4 Results

407 In this section we apply these concepts to the data taken by MMS as summarized
 408 in Figure 2 and Table 1. Figure 4 shows all the estimators discussed in the preceding sec-
 409 tion. The ambipolar and Liouville-mapped potentials (ϕ^{amb} and ϕ^{LvI0}) agree well with
 410 one another. This is not surprising as they both are proxies for the overall inflation of
 411 $f(v)$, although the very detailed match seen in panel (e) is perhaps not guaranteed given
 412 that one is an integral. These two electron-based potentials provide the standard against
 413 which all the other forms involving electric field measurements should be tested (Comișel
 414 et al., 2015; Marghitu et al., 2017). For all integrated potentials, we choose a common
 415 point at the base of the shock ramp ($t \sim 19 : 39 : 43$) to be $\phi = 0$. Several of the po-
 416 tentials drift away from being constant farther upstream or downstream. This drift could
 417 be indicative of small offsets in the measured fields, as discussed further below. There
 418 is no a priori reason for such offsets to be constant across the entire interval under in-
 419 vestigation.

420 We preface this section with a note of caution. It is not possible to separate com-
 421 pletely the limitations of approaches that employ the DC electric field measurements for
 422 the HT transformation velocities and resulting integrations of those fields from the un-
 423 certainties related to the measurement and calibration of the fields themselves.

424 Panel (b) of Figure 4 reveals that the fully time-dependent extension of the adap-
 425 tive HT concepts developed by C&M results in large discrete steps in the integrated po-
 426 tential ϕ^{AHTt} (magenta curve). Much of this curve extends beyond the limits of the panel.
 427 These steps can be traced to locations where the normal component $B_n(t)$ of the mag-
 428 netic field approaches or passes through zero. At these locations, the adaptive HT trans-

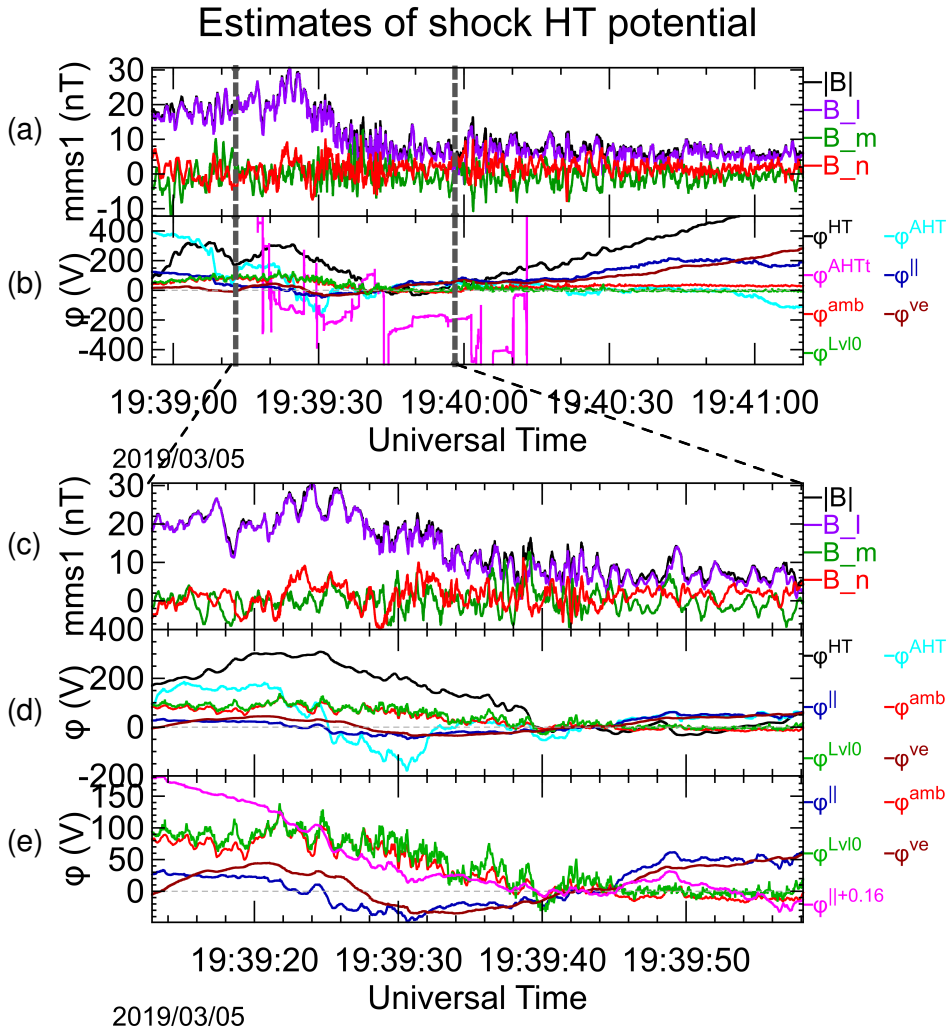


Figure 4. Comparison of different estimators for the HT potential profile through the shock shown in Figure 2, with the magnetic field for reference in panels (a) and (c). Panel (b) plots all seven estimators enumerated in the preceding section. The bottom set of panels focuses on the region in the vicinity of the main shock ramp. Panel (e) includes a re-calculation (magenta) of $\phi^{||}$ after adding a constant offset of $+0.16$ mV/m to $E_{||}$. Note that all integrated potentials have employed integration constants to make the potentials zero at the base of the shock ramp, i.e., at 19:39:43.

429 formation velocity (Equation (15) with B_n^{up} replaced by $B_n(t)$), the field is locally tan-
 430 gent to the shock surface, and the path along the field becomes infinite. These condi-
 431 tions cannot occur in strictly 1D simulations where B_n is constant in space and time.

432 The more conservative application of C&M’s adaptive HT transformation results
 433 in ϕ^{AHT} (cyan). This treats B_n as constant, drawn from the undisturbed upstream en-
 434 vironment. This clearly deviates from the strict objective of C&M’s analysis, namely to
 435 make the tangential electric field vanish or, equivalently, to make the local electron bulk
 436 velocity aligned with the magnetic field. These remnant tangential fields could be the
 437 result of non-planarity (e.g. shock ripples Lowe and Burgess (2003); Johlander et al. (2016)),
 438 time dependence or both in more realistic 2D or 3D time-dependent shocks. Figure 4d
 439 shows that this ϕ^{AHT} is larger in magnitude than the electron estimators, with a deep
 440 negative excursion within the shock ramp. The main potential change of 400 V is com-
 441 parable to that in the classic constant V^{HT} approach (black) from Equation (12).

442 Two estimators do not involve directly a HT transformation, but instead work with
 443 estimators of E_{\parallel} . They either integrate E_{\parallel} directly (ϕ^{\parallel} - blue) or effectively transform
 444 into the electron frame of reference (ϕ^{ve} - brown). Interestingly these two estimators agree
 445 with one another, demonstrating that the instrumental cross-calibrations are good and
 446 that the parallel component of the general \mathbf{E} agrees well with the specialized E_{\parallel} data
 447 product. Their main change through the steepest part of the shock ramp of ~ 80 V is
 448 comparable to that found by the electron estimators ϕ^{amb} and ϕ^{Lv10} . As shown in the
 449 magenta trace in Figure 4e, adding a constant offset of 0.16 mV/m to the experimental
 450 determination of E_{\parallel} flattens the profile of ϕ^{\parallel} upstream of the shock and brings the po-
 451 tential profile into agreement with ϕ^{amb} . This same parallel offset would apply to ϕ^{ve} .

452 5 Discussion

453 The results of this work can be grouped into three categories of estimators for the
 454 HT potential profile across a shock:

455 Electron ambipolar (ϕ^{amb}) and kinetic (ϕ^{Lv10}) estimators probe directly the elec-
 456 tron pressure gradient source of the electric field in the HT frame via the electron fluid
 457 equation and its influence on the motion of individual electrons that traverse the shock
 458 via the Vlasov equation and Liouville’s Theorem. These two estimators agree extremely
 459 well with one another in the MMS data presented here. Neither relies on details of the

460 shock parameters or motion (with the exception of the normal direction for ϕ^{amb} as dis-
 461 cussed below) nor transformation to a shock rest frame. This makes these estimators in-
 462 sensitive to knowledge of or errors in the shock and ambient plasma conditions.

463 The Liouville technique is powerful. It convolves details of the particle distribu-
 464 tion over a restricted range of energies and phase space. It is the standard used by C&M,
 465 and historically. Liouville mapping also provides indications of regions in phase space
 466 where other processes may play significant roles in shaping or energizing electrons.

467 The ambipolar estimator requires good moments of the full electron distribution,
 468 and assumptions concerning the off-diagonal elements of $\underline{\underline{P}}_e$. Technically, it also requires
 469 determination of the shock normal. In practise, since the electron pressure is nearly isotropic,
 470 this is of secondary importance. Although this is an integrated potential, it is the inte-
 471 gral of a weighted time derivative and does not suffer the same kinds of drifts seen in
 472 electric field methods below.

473 The second group of estimators focus on extracting the parallel electric field via
 474 either its direct measurement (leading to ϕ^{\parallel}) or a calculation of the electric field in the
 475 frame of the electron fluid (leading to ϕ^{ve}), essentially by evaluating the left hand side
 476 of the electron momentum equation (1). These two methods also agree well with one an-
 477 other. They do not immediately agree with the electron-only estimators ϕ^{amb} and ϕ^{Lv10}
 478 although they do show a similar increase across the steepest portion of the shock ramp.
 479 It is also clear that there is a systematic drift in these potentials from the tilted nature
 480 of their upstream profiles in Figure 4b,e. This drift is likely the result of a baseline off-
 481 set that was not fully corrected in calibration of E_{\parallel} ; adding a constant $\Delta E_{\parallel} \sim +0.16$ mV/m,
 482 which is within the uncertainty of the baseline offset in \mathbf{E} (see Section 2), would rotate
 483 the ϕ^{\parallel} trace in Figure 4 and bring these closer to the other two traces in that panel, as
 484 demonstrated by the magenta trace in Figure 4e.

485 The third group of estimators involve transforms by a tangential velocity $\mathbf{V}^{T,\alpha}$ into
 486 an HT frame in which the tangential electric field vanishes. C&M have shown already
 487 that the traditional approach (cf our ϕ^{HT}), which makes the constant asymptotic up-
 488 stream tangential field vanish, does not do a good job in the case of 1D time-dependent
 489 particle in cell simulations. Its shortcomings in the present work (ϕ^{HT}) are therefore not
 490 surprising. Their adaptive HT approach works well in their simulations, where the shock
 491 is strictly planar and the normal component B_n is constant. Applying their approach

492 in this manner, with constant $B_n = B_n^{up}$, to real data shows that these assumptions
 493 do not work well in practise (ϕ^{AHT}). We have explored an extension of their work, to
 494 allow for the temporal variations of B_n , but not the direction of the normal vector \mathbf{n} it-
 495 self. That result (ϕ^{AHTt}) contains large jumps in ϕ that can be attributed to locations
 496 where $B_n(t)$ passes close to/through zero. Our discussion following the derivation of these
 497 adaptive forms in Section 3.2 anticipated the difficulties of the adaptive forms due to such
 498 locations and/or to the incomplete cancellation of the NIF electric field.

499 6 Conclusions

500 In this paper we have investigated methods for determining experimentally the elec-
 501 trostatic potential profile across collisionless shocks, concentrating on the contribution
 502 from the frame-invariant electric field parallel to the magnetic field. This potential is known
 503 as the deHoffmann-Teller (HT) potential since, in idealized 1D, steady shocks it corre-
 504 sponds to that measured in the deHoffmann-Teller frame (de Hoffmann & Teller, 1950)
 505 in which the upstream, and downstream, flows are field-aligned and hence the $\mathbf{B} \times \mathbf{V}$
 506 motional electric field, which is the only field tangential to such shocks, vanishes. We have
 507 exploited state-of-the-art in situ plasma and field data from the NASA MMS mission.
 508 Our results provide answers to two key questions:

509 In the case of non-ideal, temporally and spatially varying conditions, does the adap-
 510 tive HT transform put forward by Comişel et al. (2015) and elaborated in Marghitu et
 511 al. (2017) offer the same improvements that it appears to do in 1D time-dependent par-
 512 ticle in cell simulations? Irrespective of the quality of the electric field data, our anal-
 513 ysis reveals short-comings of this adaptive approach that arise from the non-constant na-
 514 ture of the normal component of the magnetic field in 2D or 3D time-varying shocks. We
 515 explored further extensions of these adaptive ideas without success. There may be ad-
 516 ditional algorithms which could further extend this approach, but we are not aware of
 517 any.

518 Is it possible to measure particle and field parameters with sufficient accuracy to
 519 make reliable estimates of the integrated quasi-DC potential profile across collisionless
 520 shocks? Our results suggest a qualified “no” answer here. For some of our estimators,
 521 it is not possible to disentangle data quality/calibration issues from those related to as-
 522 sumptions of the various adaptive HT schemes. Algorithms that utilize a direct measure

523 of the frame-invariant parallel electric field, either directly as a specialized data prod-
524 uct or indirectly by transforming into the electron bulk flow frame (which requires high
525 quality electron velocity-space moments), show variations with the right size and char-
526 acter, but superimposed on a larger scale DC component that may be attributable to
527 small baseline offsets that remain after calibration. However, we would stress here the
528 difficulties in calibrating DC field measurements in the highly variable conditions found
529 in space, and also in particular across boundaries separating very different plasma con-
530 ditions. In this sense, weaker interplanetary shocks, which take less time to go past the
531 spacecraft and which have smaller changes in plasma parameters, provide more reliable
532 fields measurements (Cohen et al., 2019).

533 We have used two standard methods as our prime measures of HT potentials. One
534 used Liouville’s theorem to map electron trajectories from the upstream to the down-
535 stream populations. This technique makes few demands on the particle and field mea-
536 surements other than a consistent phase space calibration over a restricted range of en-
537 ergies and phase space densities, and the use of magnetic field data to determine the dis-
538 tribution in pitch angles. The field-aligned electrons are sufficient for this purpose, but
539 the full pitch-angle space can also be employed (Lefebvre et al., 2007). The other method
540 integrates the gradient in electron pressure, with some assumptions about gyrotropy and
541 off-diagonal elements. These two methods are quite stable and agree quantitatively with
542 one another. This agreement highlights the excellent quality of the MMS FPI data, al-
543 though previous studies have been done many times with good success (Scudder, Man-
544 geney, Lacombe, Harvey, Wu, & Anderson, 1986; Lefebvre et al., 2007; Cohen et al., 2019).

545 This work is based on the premise that the dominant influence on the electron phase
546 space inflation at collisionless shocks is the result of electron interaction with DC shock
547 fields. This idea, first put forward by Feldman et al. (1983) and then developed further
548 (Scudder, Mangeney, Lacombe, Harvey, Wu, & Anderson, 1986) and applied (Schwartz
549 et al., 1988; Lefebvre et al., 2007) (see Scudder (1995) for a review), is consistent with
550 the reported electron beams seen within the shock transition and, e.g., the coherent re-
551 flection of ions at quasi-perpendicular shocks (Paschmann et al., 1982; Madanian et al.,
552 2021). These processes point to the presence of coherent, DC fields.

553 We have assumed throughout that electrons remain magnetized through the shock
554 layer. Typically this is a good assumption, although some crossings or sub-structures may
555 violate this assumption (Schwartz et al., 2011; Balikhin et al., 1993; See et al., 2013).

556 It is clear that waves or other scattering processes are required to fill in voids left
557 in electron velocity space (Scudder, Mangeney, Lacombe, Harvey, Wu, & Anderson, 1986)
558 and to account for other distortions or features seen in the data. Shocks are known lo-
559 cations for a plethora of wave modes (K. A. Goodrich et al., 2018). Some work suggests
560 that most if not all the electron phase space inflation, often referred to simply as heat-
561 ing, can be attributed to wave-particle interactions (Wilson et al., 2014; Stasiewicz &
562 Eliasson, 2020) combined perhaps with magnetic pumping (Lichko & Egedal, 2020). Other
563 work has concentrated on short-scale electrostatic structures within the shock transition
564 (Chen et al., 2018). These structures are more amenable to direct DC field measurements,
565 and may also be the building blocks of the overall shock profile, bridging the AC and DC
566 worlds.

567 Future work will need to assemble all parts of this puzzle, which lies at the heart
568 of the dynamics and energy partition at collisionless shocks. If electric field data on its
569 own could be used to determine the HT potential profile with sufficient accuracy and cer-
570 tainty, mapping electron trajectories through that potential would point to regions in
571 phase space where discrepancies would implicate specific electron-kinetic wave modes,
572 nonlinear structures or other physical processes by their kinetic signatures. Our conclu-
573 sion that direct integration of the measured electric fields is difficult to achieve with the
574 necessary certainty nonetheless points to the need to examine fine details of the electron
575 phase space distributions themselves for clues to help address this problem.

576 **Acknowledgments**

577 ARTEMIS and Wind data were drawn from the SPDF/CDAWEB repository ([https://
578 cdaweb.gsfc.nasa.gov/index.html/](https://cdaweb.gsfc.nasa.gov/index.html/)). We gratefully acknowledge the respective in-
579 strument teams and archive curators. MMS data can be found at the MMS public Sci-
580 ence Data Center (<https://lasp.colorado.edu/mms/sdc/public/>). All the data anal-
581 ysis and graphics were performed using the opensource QSAS Science Analysis System
582 (<https://sourceforge.net/projects/qsas/>). Several of us are grateful to ISSI, Bern,
583 for their support of a Working Team. This work was supported by NASA Award 80NSSC19K0849

584 together with NASA MMS contracts to the instrument teams. IG is supported by a Royal
585 Society URF.

586 References

- 587 Angelopoulos, V. (2010). The ARTEMIS mission. In *The ARTEMIS mission* (pp.
588 3–25). Springer New York. Retrieved from [https://doi.org/10.1007/978-1-](https://doi.org/10.1007/978-1-4614-9554-3_2)
589 [4614-9554-3_2](https://doi.org/10.1007/978-1-4614-9554-3_2) doi: 10.1007/978-1-4614-9554-3_2
- 590 Balikhin, M., Gedalin, M., & Petrukovich, A. (1993, March). New mechanism for
591 electron heating in shocks. *Phys. Rev. Lett.*, *70*(9), 1259-1262. doi: 10.1103/
592 PhysRevLett.70.1259
- 593 Burch, J. L., Moore, T. E., Torbert, R. B., & Giles, B. L. (2016, March). Magne-
594 tospHERic Multiscale Overview and Science Objectives. *Space Sci. Rev.*, *199*, 5-
595 21. doi: 10.1007/s11214-015-0164-9
- 596 Burgess, D., & Scholer, M. (2015). *Collisionless Shocks in Space Plasmas*. Cam-
597 bridge University Press.
- 598 Chen, L. J., Wang, S., Wilson, L. B., Schwartz, S., Bessho, N., Moore, T., ...
599 Avanov, L. (2018, June). Electron Bulk Acceleration and Thermalization
600 at Earth's Quasiperpendicular Bow Shock. *Phys. Rev. Lett.*, *120*(22), 225101.
601 doi: 10.1103/PhysRevLett.120.225101
- 602 Cohen, I. J., Schwartz, S. J., Goodrich, K. A., Ahmadi, N., Ergun, R. E., Fuse-
603 lier, S. A., ... Burch, J. L. (2019, June). High-Resolution Measurements
604 of the Cross-Shock Potential, Ion Reflection, and Electron Heating at an In-
605 terplanetary Shock by MMS. *J. Geophys. Res.*, *124*(6), 3961-3978. doi:
606 10.1029/2018JA026197
- 607 Comișel, H., Narita, Y., & Motschmann, U. (2015, March). Adaptation of the de
608 Hoffmann-Teller frame for quasi-perpendicular collisionless shocks. *Ann. Geo-*
609 *phys.*, *33*(3), 345-350. doi: 10.5194/angeo-33-345-2015
- 610 de Hoffmann, F., & Teller, E. (1950, November). Magneto-Hydrodynamic Shocks.
611 *Phys. Rev.*, *80*(4), 692-703. doi: 10.1103/PhysRev.80.692
- 612 Dimmock, A. P., Balikhin, M. A., Krasnoselskikh, V. V., Walker, S. N., Bale,
613 S. D., & Hobara, Y. (2012, February). A statistical study of the cross-
614 shock electric potential at low Mach number, quasi-perpendicular bow shock
615 crossings using Cluster data. *J. Geophys. Res.*, *117*(A2), A02210. doi:

- 616 10.1029/2011JA017089
- 617 Ergun, R. E., Tucker, S., Westfall, J., Goodrich, K. A., Malaspina, D. M., Summers,
618 D., . . . Cully, C. M. (2016, March). The Axial Double Probe and Fields
619 Signal Processing for the MMS Mission. *Space Sci. Rev.*, *199*, 167-188. doi:
620 10.1007/s11214-014-0115-x
- 621 Feldman, W. C., Anderson, R. C., Bame, S. J., Gary, S. P., Gosling, J. T., Mc-
622 Comas, D. J., . . . Hoppe, M. M. (1983, Jan). Electron velocity distribu-
623 tions near the earth's bow shock. *J. Geophys. Res.*, *88*(A1), 96-110. doi:
624 10.1029/JA088iA01p00096
- 625 Goodrich, C. C., & Scudder, J. D. (1984, August). The adiabatic energy change
626 of plasma electrons and the frame dependence of the cross-shock potential at
627 collisionless magnetosonic shock waves. *J. Geophys. Res.*, *89*(A8), 6654-6662.
628 doi: 10.1029/JA089iA08p06654
- 629 Goodrich, K. A., Ergun, R., Schwartz, S. J., Wilson, L. B., Newman, D., Wilder,
630 F. D., . . . Andersson, L. (2018, November). MMS Observations of Elec-
631 trostatic Waves in an Oblique Shock Crossing. *J. Geophys. Res.*, *123*(11),
632 9430-9442. doi: 10.1029/2018JA025830
- 633 Hanson, E. L. M., Agapitov, O. V., Mozer, F. S., Krasnoselskikh, V., Bale, S. D.,
634 Avanov, L., . . . Giles, B. (2019, March). Cross-Shock Potential in Rippled
635 Versus Planar Quasi-Perpendicular Shocks Observed by MMS. *Geophys. Res.*
636 *Lett.*, *46*(5), 2381-2389. doi: 10.1029/2018GL080240
- 637 Harten, R., & Clark, K. (1995, February). The Design Features of the GGS Wind
638 and Polar Spacecraft. *Sp. Sci. Rev.*, *71*(1-4), 23-40. doi: 10.1007/BF00751324
- 639 Johlander, A., Schwartz, S. J., Vaivads, A., Khotyaintsev, Y. V., Gingell, I., Peng,
640 I. B., . . . Burch, J. L. (2016, October). Rippled Quasiperpendicular Shock Ob-
641 served by the Magnetospheric Multiscale Spacecraft. *Phys. Rev. Lett.*, *117*(16),
642 165101. doi: 10.1103/PhysRevLett.117.165101
- 643 Khrabrov, A. V., & Sonnerup, B. U. Ö. (1998, January). DeHoffmann-Teller Analy-
644 sis. *ISSI Scientific Reports Series*, *1*, 221-248.
- 645 Krasnoselskikh, V., Balikhin, M., Walker, S. N., Schwartz, S. J., Sundkvist, D.,
646 Lobzin, V., . . . Comisel, H. (2013, October). The Dynamic Quasiperpen-
647 dicular Shock: Cluster Discoveries. *Sp. Sci. Rev.*, *178*(2-4), 535-598. doi:
648 10.1007/s11214-013-9972-y

- 649 Kucharek, H., Möbius, E., Li, W., Farrugia, C. J., Popecki, M. A., Galvin, A. B.,
650 ... Bochsler, P. A. (2003, October). On the source and acceleration of en-
651 ergetic He⁺: A long-term observation with ACE/SEPICA. *J. Geophys. Res.*,
652 108(A10), 8040. doi: 10.1029/2003JA009938
- 653 Lefebvre, B., Schwartz, S. J., Fazakerley, A. F., & Décréau, P. (2007, Septem-
654 ber). Electron dynamics and cross-shock potential at the quasi-perpendicular
655 Earth's bow shock. *J. Geophys. Res.*, 112(A9), A09212. doi: 10.1029/
656 2007JA012277
- 657 Lichko, E., & Egedal, J. (2020, June). Magnetic pumping model for energizing
658 superthermal particles applied to observations of the Earth's bow shock. *Nat.*
659 *Commun.*, 11, 2942. doi: 10.1038/s41467-020-16660-4
- 660 Lindqvist, P.-A., Olsson, G., Torbert, R. B., King, B., Granoff, M., Rau, D.,
661 ... Tucker, S. (2016, March). The Spin-Plane Double Probe Elec-
662 tric Field Instrument for MMS. *Space Sci. Rev.*, 199, 137-165. doi:
663 10.1007/s11214-014-0116-9
- 664 Lowe, R. E., & Burgess, D. (2003, March). The properties and causes of rippling in
665 quasi-perpendicular collisionless shock fronts. *Ann. Geophys.*, 21(3), 671-679.
666 doi: 10.5194/angeo-21-671-2003
- 667 Madanian, H., Desai, M. I., Schwartz, S. J., Wilson, I., L. B., Fuselier, S. A., Burch,
668 J. L., ... Lindqvist, P. A. (2021, February). The Dynamics of a High Mach
669 Number Quasi-perpendicular Shock: MMS Observations. *Astrophys. J.*,
670 908(1), 40. doi: 10.3847/1538-4357/abcb88
- 671 Marghitu, O., Comişel, H., & Scholer, M. (2017, July). On the nonstationarity of
672 collisionless shocks and its impact on deriving the cross-shock potential. *Geo-*
673 *phys. Res. Lett.*, 44(13), 6500-6507. doi: 10.1002/2017GL073241
- 674 Mitchell, J. J., & Schwartz, S. J. (2013, Dec). Nonlocal electron heating at the
675 Earth's bow shock and the role of the magnetically tangent point. *J. Geophys.*
676 *Res.*, 118(12), 7566-7575. doi: 10.1002/2013JA019226
- 677 Mitchell, J. J., & Schwartz, S. J. (2014, February). Isothermal magnetosheath elec-
678 trons due to nonlocal electron cross talk. *J. Geophys. Res.*, 119(2), 1080-1093.
679 doi: 10.1002/2013JA019211
- 680 Paschmann, G., Haaland, S. E., Phan, T. D., Sonnerup, B. U. Ö., Burch, J. L.,
681 Torbert, R. B., ... Fuselier, S. A. (2018, March). Large-Scale Survey of the

- 682 Structure of the Dayside Magnetopause by MMS. *J. Geophys. Res.*, *123*(3),
683 2018-2033. doi: 10.1002/2017JA025121
- 684 Paschmann, G., Sckopke, N., Bame, S. J., & Gosling, J. T. (1982, August). Observa-
685 tions of gyrating ions in the foot of the nearly perpendicular bow shock. *Geo-*
686 *phys. Res. Lett.*, *9*(8), 881-884. doi: 10.1029/GL009i008p00881
- 687 Pollock, C., Moore, T., Jacques, A., Burch, J., Gliese, U., Saito, Y., . . . others
688 (2016, March). Fast Plasma Investigation for Magnetospheric Multiscale. *Space*
689 *Sci. Rev.*, *199*, 331-406. doi: 10.1007/s11214-016-0245-4
- 690 Russell, C. T., Anderson, B. J., Baumjohann, W., Bromund, K. R., Dearborn,
691 D., Fischer, D., . . . Richter, I. (2016, March). The Magnetospheric Mul-
692 tiscala Magnetometers. *Space Sci. Rev.*, *199*, 189-256. doi: 10.1007/
693 s11214-014-0057-3
- 694 Schwartz, S. J. (1998, January). Shock and Discontinuity Normals, Mach Numbers,
695 and Related Parameters. *ISSI Scientific Reports Series*, *1*, 249-270.
- 696 Schwartz, S. J. (2006, June). Shocks: Commonalities in Solar-Terrestrial Chains. *Sp.*
697 *Sci. Rev.*, *124*(1-4), 333-344. doi: 10.1007/s11214-006-9093-y
- 698 Schwartz, S. J., Henley, E., Mitchell, J., & Krasnoselskikh, V. (2011, November).
699 Electron Temperature Gradient Scale at Collisionless Shocks. *Phys. Rev. Lett.*,
700 *107*(21), 215002. doi: 10.1103/PhysRevLett.107.215002
- 701 Schwartz, S. J., Thomsen, M. F., Bame, S. J., & Stansberry, J. (1988, November).
702 Electron heating and the potential jump across fast mode shocks. *J. Geophys.*
703 *Res.*, *93*, 12923-12931. doi: 10.1029/JA093iA11p12923
- 704 Schwartz, S. J., Thomsen, M. F., & Gosling, J. T. (1983, March). Ions upstream of
705 the earth's bow shock: A theoretical comparison of alternative source popula-
706 tions. *J. Geophys. Res.*, *88*(A3), 2039-2047. doi: 10.1029/JA088iA03p02039
- 707 Schwartz, S. J., Zweibel, E. G., & Goldman, M. (2013, October). Microphysics in
708 Astrophysical Plasmas. *Sp. Sci. Rev.*, *178*(2-4), 81-99. doi: 10.1007/s11214-013
709 -9975-8
- 710 Scudder, J. D. (1987, December). The field-aligned flow approximation for
711 electrons within layers possessing a normal mass flux: A corollary to the
712 deHoffmann-Teller theorem. *J. Geophys. Res.*, *92*(A12), 13447-13455. doi:
713 10.1029/JA092iA12p13447
- 714 Scudder, J. D. (1995, February). A review of the physics of electron heating at colli-

- 715 collisionless shocks. *Adv. Space Res.*, *15*(8-9), 181-223. doi: 10.1016/0273-1177(94)
716 00101-6
- 717 Scudder, J. D., Mangeney, A., Lacombe, C., Harvey, C. C., Aggson, T. L., Anderson,
718 R. R., . . . Russell, C. T. (1986, October). The resolved layer of a collisionless,
719 high β , supercritical, quasi-perpendicular shock wave 1. Rankine-Hugoniot
720 geometry, currents, and stationarity. *J. Geophys. Res.*, *91*(A10), 11019-11052.
721 doi: 10.1029/JA091iA10p11019
- 722 Scudder, J. D., Mangeney, A., Lacombe, C., Harvey, C. C., Wu, C. S., & Anderson,
723 R. R. (1986, October). The resolved layer of a collisionless, high β , supercrit-
724 ical, quasi-perpendicular shock wave, 3. Vlasov electrodynamics. *J. Geophys.*
725 *Res.*, *91*(A10), 11075-11098. doi: 10.1029/JA091iA10p11075
- 726 See, V., Cameron, R. F., & Schwartz, S. J. (2013, April). Non-adiabatic electron be-
727 haviour due to short-scale electric field structures at collisionless shock waves.
728 *Ann. Geophys.*, *31*(4), 639-646. doi: 10.5194/angeo-31-639-2013
- 729 Slavin, J. A., & Holzer, R. E. (1981, December). Solar wind flow about the ter-
730 restrial planets, 1. Modeling bow shock position and shape. *J. Geophys. Res.*,
731 *86*(A13), 11401-11418. doi: 10.1029/JA086iA13p11401
- 732 Sonnerup, B. U. Ö. (1969, January). Acceleration of particles reflected at a shock
733 front. *J. Geophys. Res.*, *74*(5), 1301. doi: 10.1029/JA074i005p01301
- 734 Stasiewicz, K., & Eliasson, B. (2020, November). Quasi-adiabatic and Stochastic
735 Heating and Particle Acceleration at Quasi-perpendicular Shocks. *Astrophys.*
736 *J.*, *903*(1), 57. doi: 10.3847/1538-4357/abb825
- 737 Stone, R. G., & Tsurutani, B. T. (1985, January). Collisionless shocks in the helio-
738 sphere. A tutorial review. *Washington DC American Geophysical Union Geo-*
739 *physical Monograph Series*, *34*. doi: 10.1029/GM034
- 740 Thomsen, M. F., Gosling, J. T., Bame, S. J., Quest, K. B., Winske, D., Livesey,
741 W. A., & Russell, C. T. (1987, March). On the noncoplanarity of the magnetic
742 field within a fast collisionless shock. *J. Geophys. Res.*, *92*(A3), 2305-2314. doi:
743 10.1029/JA092iA03p02305
- 744 Thomsen, M. F., Mellott, M. M., Stansberry, J. A., Bame, S. J., Gosling, J. T.,
745 & Russell, C. T. (1987, September). Strong electron heating at the
746 Earth's bow shock. *J. Geophys. Res.*, *92*(A9), 10119-10124. doi: 10.1029/
747 JA092iA09p10119

- 748 Thomsen, M. F., Schwartz, S. J., & Gosling, J. T. (1983, October). Observational
 749 evidence on the origin of ions upstream of the earth's bow shock. *J. Geophys.*
 750 *Res.*, *88*(A10), 7843-7852. doi: 10.1029/JA088iA10p07843
- 751 Torbert, R. B., Russell, C. T., Magnes, W., Ergun, R. E., Lindqvist, P.-A., LeCon-
 752 tel, O., ... Lappalainen, K. (2016, March). The FIELDS Instrument Suite
 753 on MMS: Scientific Objectives, Measurements, and Data Products. *Space Sci.*
 754 *Rev.*, *199*, 105-135. doi: 10.1007/s11214-014-0109-8
- 755 Tsurutani, B. T., & Stone, R. G. (1985, January). Collisionless shocks in the he-
 756 liosphere: Reviews of current research. *Washington DC American Geophysical*
 757 *Union Geophysical Monograph Series*, *35*. doi: 10.1029/GM035
- 758 Wilson, L. B., Brosius, A., Gopalswamy, N., Nieves-Chinchilla, T., Szabo, A.,
 759 Hurley, K. C., ... TenBarge, J. M. (2021, January). A quarter century
 760 of wind spacecraft discoveries. *under review for Reviews of Geophysics.*
 761 Retrieved from <https://doi.org/10.1002/essoar.10504309.2> doi:
 762 10.1002/essoar.10504309.2
- 763 Wilson, L. B., Chen, L.-J., & Roytershteyn, V. (2021, January). The discrepancy be-
 764 tween simulation and observation of electric fields in collisionless shocks. *Fron-*
 765 *tiers in Astronomy and Space Sciences*, *7*, 97. doi: 10.3389/fspas.2020.592634
- 766 Wilson, L. B., Sibeck, D. G., Breneman, A. W., Le Contel, O., Cully, C., Turner,
 767 D. L., ... Malaspina, D. M. (2014, August). Quantified energy dissipation
 768 rates in the terrestrial bow shock: 2. Waves and dissipation. *J. Geophys. Res.*,
 769 *119*(8), 6475-6495. doi: 10.1002/2014JA019930
- 770 Wu, C. S. (1984, October). A fast Fermi process: Energetic electrons accelerated by
 771 a nearly perpendicular bow shock. *J. Geophys. Res.*, *89*(A10), 8857-8862. doi:
 772 10.1029/JA089iA10p08857